



Numerical investigation of heat transfer enhancement in a dimpled cooling channel with different angles of the vortex generator

Myunggeun Jeong^a, Man Yeong Ha^{a,*}, Yong Gap Park^{b,*}

^aSchool of Mechanical Engineering, Pusan National University, Jang Jeon 2-Dong, Geumjeong-gu, Busan 609-735, Republic of Korea

^bRolls-Royce and Pusan National University Technology Centre in Thermal Management, Jang Jeon 2-Dong, Geumjeong-gu, Busan 609-735, Republic of Korea



ARTICLE INFO

Article history:

Received 4 March 2019

Received in revised form 23 August 2019

Accepted 25 August 2019

Keywords:

Dimpled cooling channel
Heat transfer enhancement
Vortex generator
Direct numerical simulation

ABSTRACT

This study carried out numerical simulations to investigate the flow and heat transfer characteristics for air flowing in a dimpled cooling channel with a vortex generator. A crescent-shaped protrusion was mounted as a vortex generator on the downstream of the dimple. A direct numerical simulation (DNS) was conducted in a dimpled cooling channel with a Reynolds number of 2800. Seven different cases were considered, including one general dimpled wall and dimpled wall with six different angles inside the vortex generator. For the vortex generator mounted cases, the main design variable is the angle inside the vortex generator, which varies from 0 to 75°. The normalized thermo-performance factors were calculated to estimate the performance of the cooling channel. The normalized thermo-performance factors f/f_0 , j/j_0 , and the volume goodness factor decreases as θ increases. The dimpled channel with a vortex generator shows better normalized thermo-performances than the general dimpled channel.

© 2019 Elsevier Ltd. All rights reserved.

1. Introduction

Recently, interest in improving the energy efficiency has increased by global warming in a wide range of industrial fields. There are a number of ways to improve the energy efficiency, such as reduce weight using composite material for vehicles, switching to light emitting diode (LED) lamps, and improving the performance of heat exchangers. Heat exchangers are one of the main components in the industry fields to improve the efficiency.

Previous studies have been conducted to improve the performance of heat exchangers using passive methods based on mixing the fluid layers with the core flow and increasing the surface area. Passive methods do not need any external power source, in contrast to active methods. Therefore, passive methods are widely used for many engineering applications. Passive methods use many techniques to enhance the heat transfer, such as pin fins, louvered fins, corrugated tubes, wire coil inserts, and dimpled surfaces. Dimpled surfaces have been shown to increase heat transfer performance with a low pressure drop compared to other types of passive methods. Therefore, many researchers have investigated to determine the flow and heat transfer characteristics generated by a dimpled wall.

Wang et al. [1] conducted numerical simulations to study turbulent flows in a dimpled channel in a Reynolds number range of 3000 to 6000 with various channel geometries. The dimpled channels had large pressure drop by the presence of dimples compared to a smooth channel. Nesselrooji et al. [2] experimentally investigated the drag and flow structure caused by surfaces with patterns of dimples with various Reynolds numbers. They reported that dimples in the channel lead to drag reduction by affecting the turbulence structures in the boundary layer. Elyyan et al. [3,4] carried out direct and large eddy simulations in dimple and protrusion channels with Reynolds numbers in the range of 200–15,000 under different channel heights. They reported that the smaller channel height is more appropriate in the low Reynolds number regime, which is corresponding to the typical operating condition of compact heat exchangers. The dimple and protrusion channels were competitive with other augmentation surface in the turbulent regime, regardless of the channel height. Moreover, they analysis the contributions of form and friction drag to the loss according to the channel heights and Reynolds numbers. Ligrani and his co-workers [5–8] investigated the effects of dimple depth on the flow and heat transfer characteristics with various Reynolds numbers. They concluded that the strength of the vortices, turbulence transport and turbulence production increases with increasing dimple depth. As a result, the friction factor and Nusselt number increase with increasing dimple depth. According to these studies [1–8], the flow characteristics and heat transfer performance of the dimpled

* Corresponding authors.

E-mail addresses: myha@pusan.ac.kr (M.Y. Ha), pyg777@pusan.ac.kr (Y.G. Park).

Nomenclature

A	area	x, y, z	Cartesian coordinates
C_p	pressure coefficient		
D	dimensionless dimple-imprinted diameter		
d	dimensionless diameter of vortex generator		
D_h	hydraulic diameter		
D_p	form drag		
D_f	friction drag		
f	Fanning friction factor		
G_v	volume goodness factor		
H	channel height		
h	dimensionless height of vortex generator		
j	Colburn j factor		
L	length of computational domain		
Nu	Nusselt number		
p	dimensionless pressure		
Pr	Prandtl number		
Re	Reynolds number		
St	Stanton number		
t	dimensionless time		
T	dimensionless temperature		
V	volume of computational domain		
\mathbf{u}	dimensionless velocity vectors		
w_{vg}	dimensionless width of the gap inside the vortex generator		
W	width of computational domain		
			<i>Greek symbols</i>
			α thermal diffusivity
			δ dimensionless dimple-imprinted depth
			λ_2 lamda-2 criteria for vortical structure
			ν kinematic viscosity
			ρ fluid density
			Π dimensionless mean pressure gradient
			θ angle inside the vortex generator
			<i>Subscripts</i>
			0 general dimple case
			ht heat transfer surface
			<i>Superscripts</i>
			$*$ dimensional quantity
			$+$ wall coordinate
			<i>Mathematical symbols</i>
			$-$ time-averaged quantity
			$\langle \rangle$ surface-averaged quantity

surface is strongly dependent on the operating flow conditions and geometry of the channel.

Lan et al. [9] numerically studied the flow and heat transfer characteristics in a rectangular microchannel with dimples and protrusions with Reynolds numbers in the range of 100–900. The Nusselt number in the microchannel increased from 1.12 to 4.77 times compared to that of a smooth channel. The corresponding friction factor increased from 0.94 to 2.03 times that of the smooth channel. They also reported that staggered cases have better thermal performance than the non-staggered cases.

Sato et al. [10] conducted large eddy simulations of a dimpled channel to investigate the effect of the Prandtl number on the heat transfer performance. Numerical simulations were conducted with Reynolds numbers in the range of 1000–10600 and Prandtl numbers in the range of 0.2–3.0. The best performance occurred at $Re = 2000$ and $Pr = 3.0$ in terms of the heat transfer and pressure drop. The heat transfer efficiency was strongly dependent on not only the operating flow conditions but also the thermo-physical properties of the working fluid. They suggested that it is important to design dimpled channel of appropriate size to increase the heat transfer performance.

Numerous studies have investigated augmented dimpled surfaces to enhance the heat transfer capacity [11–17]. Xie et al. [11] investigated the flow and heat transfer characteristics of tear-drop dimples with different eccentricities in a Reynolds number range of 3000–9000. The ratios of the eccentricity and hydraulic diameter (e/D_h) were varied from 0 to 0.4. The poorest thermal performance occurred at $e/D_h = 0.1$, which gradually increased as the center of the tear-drop dimple moved downwards for $e/D_h > 0.1$. Yoon et al. [12] numerically investigated the flow and heat transfer characteristics in a channel with a tear-drop dimple on the bottom wall with a Reynolds number of 2800. The pressure loss and heat transfer were influenced by the spanwise circulation and streamwise swirling motion resulting from the tear-drop dimple. They compared the thermo-hydraulic performance of tear-drop dimple with that of general dimple and found that the

tear-drop dimple shape is more advantages. The tear-drop dimple showed good energy savings and heat transfer enhancement for lower Reynolds numbers, as reported by Xie et al. [11] and Yoon et al. [12].

Jordan and Wright [13] experimentally investigated the effect of the Reynolds number on the heat transfer and thermal performance of V-shaped dimples in a rectangular channel. At lower Reynolds numbers, the V-shaped dimples showed similar heat transfer and pressure drop behavior to that of general dimples. However, at higher Reynolds numbers, the heat transfer capacity of V-shaped dimples was enhanced with increasing Reynolds number. As the Reynolds number increased, the heat transfer capacity was increased by the counter-rotating vortices induced by the dimples. They predicted that the V-shaped dimple design could replace the conventional ribs or hemispherical dimples due to the thermal performance at high Reynolds numbers.

Xie et al. [14] determined the optimal configurations for augmenting the surface heat transfer rates for different shapes of dimples. The shapes of dimples were general dimples, elliptical dimples, egg-shaped dimples, and super-spherical dimples. The flow and thermal characteristics were obtained using computational fluid dynamics in a Reynolds number range of 8000 to 24000. The elliptical dimples showed the best performance at lower Reynolds numbers, and the general dimple arrangement had the best performance at higher Reynolds numbers. The optimal heat transfer augmentations occurred when the largest cross-section area was oriented perpendicular to the streamwise direction since larger areas were then available for reattachment of the shear layer over downstream portions of the dimples.

Doo et al. [15] conducted a parametric study on flows passing through a channel with a combination of dimples and a riblets. They studied six different cases (a general dimpled surface and riblet-mounted dimpled surfaces with five different riblet angles). In the cases of the riblet-mounted dimpled surfaces, the pressure loss was reduced, and the heat transfer capacity was found to be same as that in case of the general dimpled surface. The highest

thermo-aerodynamic performance factor was predicted for case of the riblet-mounted dimple with a riblet angle of 60°, which was assessed in terms of the volume goodness factor. Rao et al. [16,17] investigated the heat transfer and flow characteristics in channels with arrays of a pin fin-dimple for Reynolds numbers ranging from 8200 to 50,500. Pin fin-dimple channels increase the turbulent mixing and enhance the heat transfer rate compared to the pin-fin channel. Also, the pin fin-dimple channel with deeper dimples showed higher Nusselt number distributions. In addition, the highest heat transfer region was affected by the vortex flow characteristics according to the Reynolds number variations. The vortex characteristic has a significant effect on the heat transfer performance, as reported by Rao et al. [16,17]. Ligrani et al. [18,19] investigated the effects of longitudinal vortices with different circulations on heat transfer. According to Ligrani et al. [18,19], the vortices cause local Stanton numbers to be augmented by more than 20 percent relative with no vortices. Many studies carried out to enhance the heat transfer performance in a channel by using a vortex generator to generate the vortices.

Sinha et al. [20] simulated the air flow through fin-tube heat exchangers with rectangular winglet vortex generators. The swirling motions generated by the vortex generator disrupted the thermal boundary layer, led to flow mixing, and enhanced the heat transfer with less pressure penalty. They also concluded that the optimum configuration of the vortex generators needs to be chosen based on the Reynolds number for a particular heat exchanger application. Khoshvaght-Aliabadi et al. [21] investigated the thermal and flow characteristics of a plate-fin heat exchanger with a transverse vortex generator for Reynolds numbers ranging from 100 to 1600. The wings height, wings width, wings attach angle, wings attack angle, transverse wings pitch, and longitudinal wings pitch were considered as the design parameters. The wings height had the greatest effect on the thermal performance, among all the considered design parameters.

Tang et al. [22] carried out numerical simulations to investigate the effect of six types of longitudinal vortex generator configurations on the flow and thermal characteristics in the channels. They evaluated the thermo-hydraulic performance using the JF factor, which was defined as $j/(f^{1/3})$. For all six types of longitudinal vortex generators, the heat transfer performance was higher than that of the smooth channel. The pressure drop was also larger than that of the smooth channel in all configurations considered. The JF factors of all cases were higher than that of the smooth channel, except for the case of the conventional rectangular winglet. This result indicates that it is important to design the vortex generator while considering the thermo-hydraulic performance. Ke et al. [23] conducted numerical simulations of fluid flow and heat transfer in a channel with different delta-shaped longitudinal vortex generators and channel heights for Reynolds numbers ranging from 600 to 2200. They reported the thermal performance is highly influenced by the channel height and the aspect ratio of the vortex generator.

Luo et al. [24] investigated the effects of dimples and their arrangement on the flow and heat transfer characteristics in a channel with delta-winglet vortex generators. The Reynolds number was 4000–40,000. The combination of delta-winglet vortex generators and dimples improved the thermal performance compared to channels with only delta winglet vortex generators. Xia et al. [25] studied the flow and heat transfer in dimple heat exchangers using the lattice Boltzmann method. A small longitudinal vortex generator was used to enhance the heat transfer performance with a low pressure drop. A grooved was also placed inside the longitudinal vortex generator to reduce the pressure drop caused by the vortex generator. The results showed that the longitudinal vortex generator improved the thermal performance compared to the dimple cases.

Many previous studies have shown that dimpled channel have benefits with less pressure drop to enhance the heat transfer. In addition, the vortex generator can increase the heat transfer performance compared to a flat channel. Therefore, numerical simulations were carried out in this study to increase the cooling performance by combining of a vortex generator with a dimpled channel. However, the optimum configuration of the vortex generators needs to be chosen based on the Reynolds number for a particular heat exchanger application in terms of the pressure drop and heat transfer performance. Thus, the effect of the shape of the vortex generator on the flow and heat transfer was investigated.

A small crescent-shaped protrusion was mounted downstream of the dimple as a vortex generator to increase the heat transfer capacity. A direct numerical simulation (DNS) was conducted in a dimpled cooling channel with a Reynolds number of 2800. Thermo-performance factors were calculated to estimate the performance of the cooling channel, such as Fanning friction factor, Colburn j factor and volume goodness factor.

2. Numerical methodology

2.1. Governing equations

The governing equations used in this study are the continuity equation, momentum equation, and energy equations to simulate the flow and thermal fields. The governing equations are shown in Eqs. (1)–(3).

$$\nabla \cdot \mathbf{u} = 0 \quad (1)$$

$$\frac{\partial \mathbf{u}}{\partial t} + (\mathbf{u} \cdot \nabla) \mathbf{u} = -\nabla p + \frac{1}{Re_m} \nabla^2 \mathbf{u} + \boldsymbol{\Pi} \quad (2)$$

$$\frac{\partial T}{\partial t} + \mathbf{u} \cdot \nabla T = \frac{1}{Re_m Pr} \nabla^2 T \quad (3)$$

The dimensionless variables in Eqs. (1)–(3) are defined as dimensionless velocity, $\mathbf{u} = \mathbf{u}^*/U_m$, pressure, $p = p^*/\rho U_m^2$, temperature, $T = (T^* - T_{lower}^*) / (T_{upper}^* - T_{lower}^*)$, and time, $t = t^* U_m / H$. The superscript * denotes dimensional variables. U_m and H represent the mean bulk velocity and height of the cooling channel. T_{upper} and T_{lower} are the temperature of the upper and lower walls, respectively. In the present study, the bulk Reynolds number and Prandtl number are defined as $Re_m = U_m H / \nu$ and $Pr = \nu / \alpha$. The bulk Reynolds number and the Prandtl number were set equal 2800 and 0.71.

A two-step time-splitting method was employed in time stepping scheme as suggested by Kim and Moin [26] and Zang et al. [27]. In Eqs. (2) and (3), the convection terms were treated explicitly by the second-order Adams-Basforth method, and the second-order Crank-Nicolson scheme was used for solving diffusion terms.

Periodic boundary conditions were applied in the x - and z -directions. No-slip boundary conditions were applied on both the upper and lower walls. The temperature was fixed at the upper and lower walls as $T_{upper} = 1$ and $T_{lower} = 0$. A CFL number was used for the time advancement to satisfy the stability condition of less than 0.15.

2.2. Configurations of dimpled cooling channel

Fig. 1 shows the configurations of a “general dimpled wall” and a “dimpled wall with a vortex generator”. As shown in the left sides of **Fig. 1(a)** and (b), L , H , and W are the longitudinal length, vertical height, and transversal width of the computational domain,

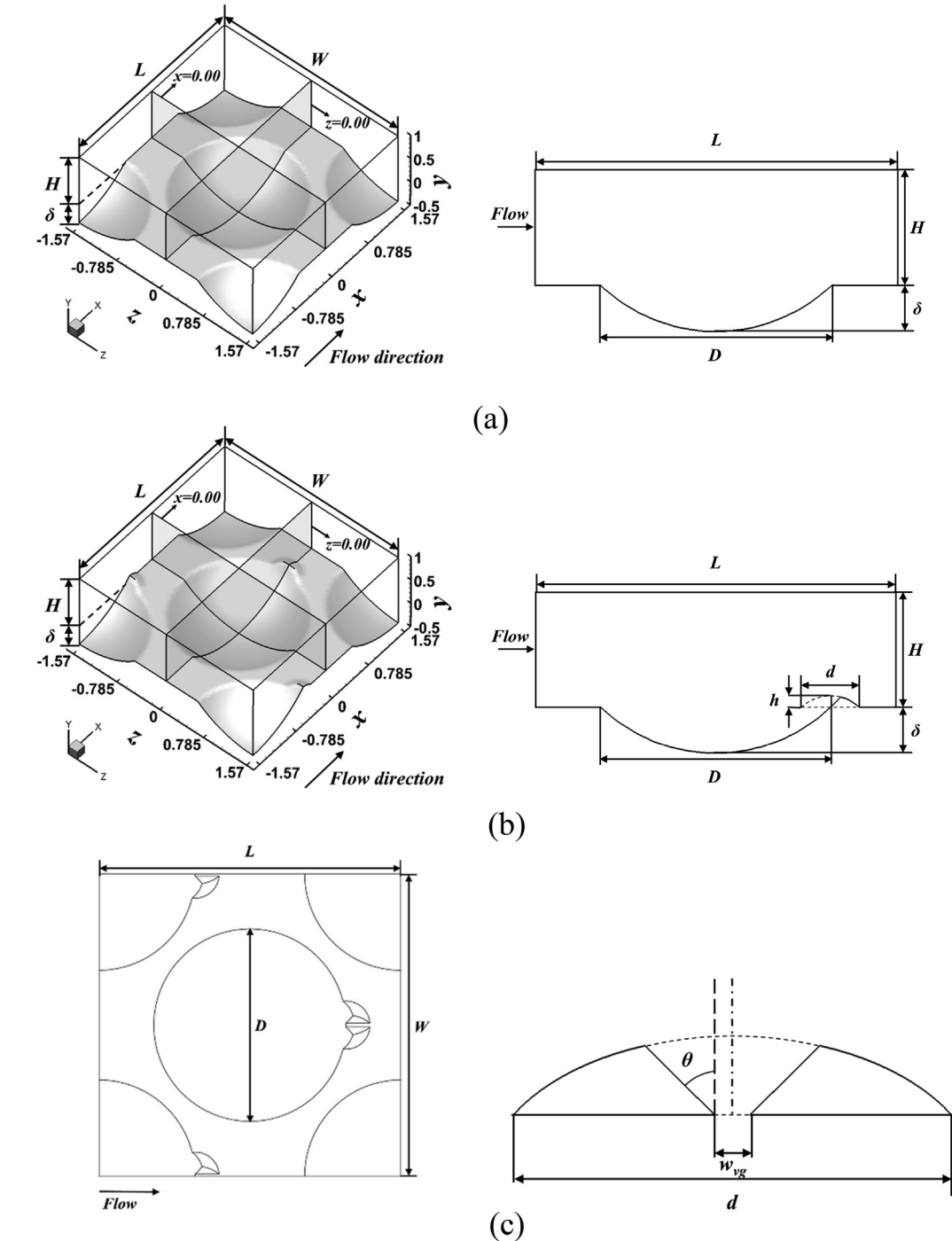


Fig. 1. Configurations with their coordinate system and dimensions of the computational domain: (a) general dimpled surface, (b) dimpled surface with a vortex generator, and (c) detailed dimensions of the vortex generator.

respectively. The right sides of Fig. 1(a) and (b) show design parameters of present study. As shown in the right sides of Fig. 1 (a) and (b), D , δ , h , and d represents the diameter of the dimple, depth of the dimple, vertical height of the vortex generator, and the diameter of the vortex generator, respectively. In the case of a general dimpled surface, the parameters associated with the vortex generator, such as h and d , are undefined. Fig. 1(c) shows the design variables of the vortex generator in detail, which is corresponding to the cases of a dimpled surface with a vortex generator. For the vortex generator mounted cases, the main design variable is the angle inside the vortex generator. As shown in the right side

of Fig. 1(c), d , w_{vg} , and θ represents the diameter of the vortex generator, width of the gap, and angle inside the vortex generator. The seven cases including one general dimpled surface and dimple surface with six different vortex generator cases were considered in the present study. The detailed dimensions for design variables applied in this study are shown in Table 1.

2.3. Computational domain size and grid resolution

The dimensions of the computational domain were $\pi \times 1 \times \pi$ corresponding to L , H , and W , respectively, which was based on

Table 1

Design variables for the cases considered.

Case no.	Dimensions ($L \times H \times W$)	D	δ	d	h	w_{vg}	θ
1	$\pi \times 1 \times \pi$	2.0	0.4	0	0	0	0
2	$\pi \times 1 \times \pi$	2.0	0.4	0.5	0.1	0	0
3	$\pi \times 1 \times \pi$	2.0	0.4	0.5	0.1	0.04	15°
4	$\pi \times 1 \times \pi$	2.0	0.4	0.5	0.1	0.04	30°
5	$\pi \times 1 \times \pi$	2.0	0.4	0.5	0.1	0.04	45°
6	$\pi \times 1 \times \pi$	2.0	0.4	0.5	0.1	0.04	60°
7	$\pi \times 1 \times \pi$	2.0	0.4	0.5	0.1	0.04	75°

previous research conducted by Elyyan et al. [3]. The grid dependency test was performed with an angle inside the vortex generator of 15°. The total drag and Nusselt number converged when the number of cells exceeded 804,357 as shown in Table 2. Thus, appropriate grid numbers of $93 \times 93 \times 93$ were adopted in the x -, y -, and z -directions. Fig. 2 shows the grid distribution of the computational domain at $z = 0$. The distance between wall and the first grid points is confined to $y^+ \approx 0.1$.

The results of present numerical method have been validated with the results obtained from the empirical expressions of Darcy friction factor and Nusselt number of a flat channel proposed by Petukhov and Gnielinski given in Eqs. (4) and (5). The results show a good agreement and have been tabulated in terms of Fanning friction factor and Nusselt number in Table 3.

$$f_D = [1.58\ln(Re) - 2.185]^{-2} \quad (4)$$

$$Nu = \frac{(f_D/2)(Re - 500)Pr}{1 + 12.7(f_D/2)^{1/2}(Pr^{2/3} - 1)} \quad (5)$$

Also, previous numerical simulations for the dimple channel flow problem considered by Wang et al. [1] were conducted to validate the present numerical simulation code. The results agree well with those of previous studies in terms of the Fanning friction factor, as shown in the middle part of Table 3. The lower part of Table 3 shows a comparison of the results of Yoon et al. [12] for the total drag and Nusselt number. The present results agree well with empirical and previous results, thus showing the validity of the numerical method.

2.4. Thermo-hydraulic performance metric

The form and friction drags were calculated using Eqs. (6) and (7).

$$\langle D_p \rangle = - \int_S (p + \Pi x) \vec{i} \cdot \vec{n} dS \quad (6)$$

$$\langle D_f \rangle = \int_S (\tau_{xx} \vec{i} + \tau_{yx} \vec{j} + \tau_{zx} \vec{k}) \cdot \vec{n} dS \quad (7)$$

where Π and τ are the average pressure gradient and skin shear stress on a surface, respectively.

The local and surface-averaged Nusselt number, Stanton number, Fanning friction factor, Colburn j factor, and volume goodness factor are defined as follows:

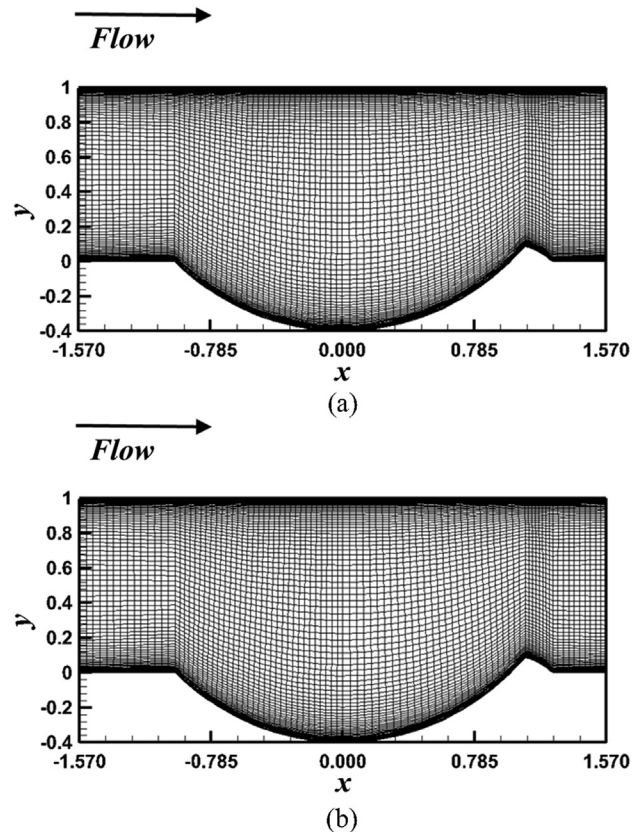


Fig. 2. Grid distribution on the spanwise-normal plane at the center of the computational domain ($z = 0$) for (a) general dimpled surface and (b) dimpled surface with a vortex generator.

$$Nu = \frac{hD_h}{k}, \quad \langle Nu \rangle = \frac{1}{S} \int_S Nu ds, \quad (8)$$

$$St = \frac{Nu}{RePr} \quad (9)$$

$$f = \frac{\Delta p D_h}{2 \rho U_m^2 L} \quad (10)$$

$$j = St Pr^{2/3} \quad (11)$$

$$G_v = St/f^{1/3} \quad (12)$$

where h , D_h , and k are the heat transfer coefficient, hydraulic diameters, and thermal conductivity. The volume goodness factor was suggested by Shah and London [28] which is a quantitative value that is widely used in heat transfer applications such as heat exchangers to evaluate the thermo-performance in different configurations. Since the large volume goodness factor requires a small

Table 2

Sensitivity analysis of the grid density for the case of $\theta = 15^\circ$.

Grids ($L \times H \times W$)	Total Grids	Total drag	Total Nusselt number
69 × 69 × 69	328,509	0.678	15.769
81 × 81 × 81	531,441	0.707	15.627
93 × 93 × 93	804,357	0.718	15.505
105 × 105 × 105	1,157,625	0.720	15.488

Table 3

Validation results with a flat channel and dimpled channels.

Cases	Re	$L \times H \times W$	F (error, %)	Total drag (error, %)	Total Nusselt number (error, %)
Empirical results Eqs. (4) and (5)	5600		1.91×10^{-3} (Ref.)	-	16.44 (Ref.)
Present study	5600	$2\pi \times 2 \times \pi$	2.03×10^{-3} (+6.3%)	-	16.32 (-0.07%)
Wang et al. [1]	3900	$\pi \times 2 \times \pi$	4.38×10^{-3} (Ref.)	-	-
Present study	3900	$\pi \times 2 \times \pi$	4.35×10^{-3} (-0.68)	-	-
Yoon et al. [13]	2800	$\pi \times 1 \times \pi$	-	0.618 (Ref.)	14.378 (Ref.)
Present study	2800	$\pi \times 1 \times \pi$	-	0.608 (-1.62)	14.032 (-2.40)

pumping power, the volume and overall weight of the heat exchanger can be reduced while maintaining the same heat transfer performance. The hydraulic diameters of each cases can be defined based on an Eq. (13) as follows:

$$D_h = \frac{4V}{A_{ht}} \quad (13)$$

where V and A_{ht} are the volume and the wetted area of the computational domain. Time- and surface-averaged drags and Nusselt number are defined as follows:

$$\overline{\langle D_p \rangle} = \frac{1}{t_p} \int_0^{t_p} \langle D_p \rangle dt \quad (14)$$

$$\overline{\langle D_f \rangle} = \frac{1}{t_p} \int_0^{t_p} \langle D_f \rangle dt \quad (15)$$

$$\overline{\langle Nu \rangle} = \frac{1}{t_p} \int_0^{t_p} \langle Nu \rangle dt \quad (16)$$

where t_p is the period of time average.

3. Results and discussion

3.1. Performance estimation

Fig. 3 shows the performance ratios f/f_0 , j/j_0 , and G_v/G_{v0} for the different shapes. The quantitative performance of the pressure drop and heat transfer can be evaluated by the Fanning friction factor and the Colburn j factor, respectively. The subscript '0' in Fig. 3 indicates the thermo-performance of a general dimpled case.

The pressure drop in terms of f/f_0 is about 21% greater for $\theta = 0^\circ$ than for a general dimpled surface. f/f_0 gradually decreases as the angle inside the vortex generator increases from 15 to 75° . The normalized Fanning friction factor f/f_0 is larger than 1.0 for all cases

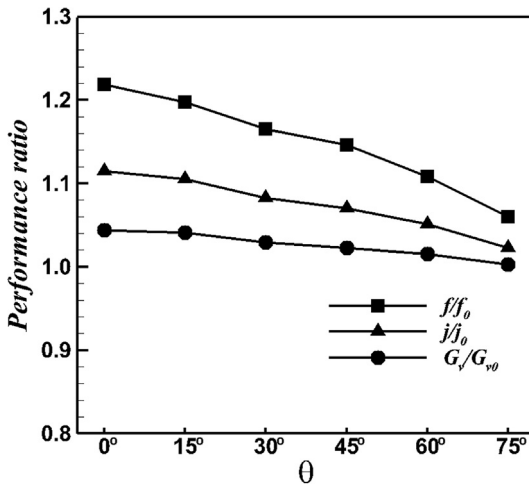


Fig. 3. Variations in the three different thermo-hydraulic performance parameters.

with the vortex generator. This means that the pressure drop is greater than that of the general dimpled surface when a vortex generator is mounted. The heat transfer performance in terms of j/j_0 shows a similar graph trend to f/f_0 . In the case of $\theta = 0^\circ$, j/j_0 is about 11% larger than that of the general dimpled surface and gradually decreases as the angle inside the vortex generator increases from 15 to 75° . The normalized Colburn j factor j/j_0 is larger than 1.0 for all cases with the vortex generator. This also means that the heat transfer capacity is greater than that of the general dimpled surface when a vortex generator is present. The G_v/G_{v0} also shows a similar graph trend to f/f_0 . In the case of $\theta = 0^\circ$, the factor is about 4% larger than that of the general dimpled surface and

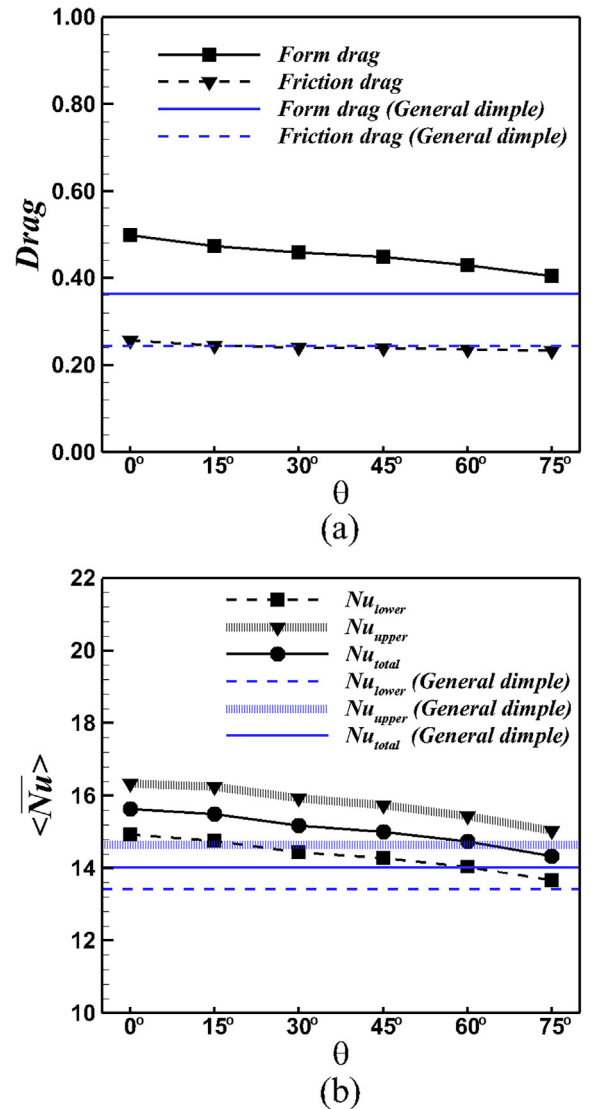


Fig. 4. Time- and surface-averaged dimensionless quantities on the upper and lower surfaces: (a) drag and (b) Nusselt number.

gradually decreases as the angle inside the vortex generator increases from 15 to 75°.

Fig. 4(a) shows the form and friction drags on the channel. Form drag, $\langle D_p \rangle$, is the force acting in the normal direction on the surface by the surface shape, whereas friction drag, $\langle D_f \rangle$, is the force acting on the surface in the tangential direction by the skin shear stress. The form drag represents the form drag due to the lower surface shape because there is a flat plate on the upper surface of the channel. The results of the general dimpled surface are indicated as a blue line. The form drag increases as the lower surface shape changes by the vortex generator compared to the general dimpled case. In the case of $\theta = 0^\circ$, the form drag increases by about 37% compared to the general dimpled case. At $\theta = 15^\circ\text{--}75^\circ$, the flow resistance due to the shape is reduced by the gap inside the vortex generator compared to the result at $\theta = 0^\circ$. Therefore, as the angle inside the vortex generator increases, the form drag gradually decreases. However, the change of the friction drag according to the shape of the lower surface is not large but almost constant. The friction drag has a small value compared to the form drag. Therefore, the pressure drop change in the channel is mainly caused by the form drag change.

The pressure force at the inlet and outlet is the force resulting from the pressure difference at the inlet and outlet. The pressure drop in the computational domain occurs by the form and friction

drags. Then, form and friction drags, and pressure force satisfy the balance equation in the computational domain. Therefore, as shown in **Figs. 3 and 4(a)**, when the total drag is large, the pressure drop is also large, and thus the Fanning friction factor has a large value. On the contrary, when the total drag is small, the Fanning friction factor has a relative small value.

Fig. 4(b) shows the time- and surface-averaged Nusselt number on the upper and lower surfaces. The results of the general dimpled surface are indicated as a line. Since the Reynolds number and the Prandtl number are constant, the Nusselt number graph shows the same graph pattern as j/j_0 . In case of $\theta = 0^\circ$, the Nusselt number is about 11% larger than that of the general dimple and gradually decreases as the angle inside the vortex generator increases from 15 to 75°.

3.2. Flow characteristics

3.2.1. Instantaneous flow fields

The vortex visualization technique proposed by Jeong and Hussain [29] was used to identify the characteristics of the turbulence structure. λ_2 is the second largest eigenvalue of $S^2 + \Omega^2$, where S^2 and Ω^2 are the strain and rotation rates of the velocity gradient tensor, respectively. The tensor determines the existence of a local pressure minimum due to vortical motions. A λ_2 of -15 was used

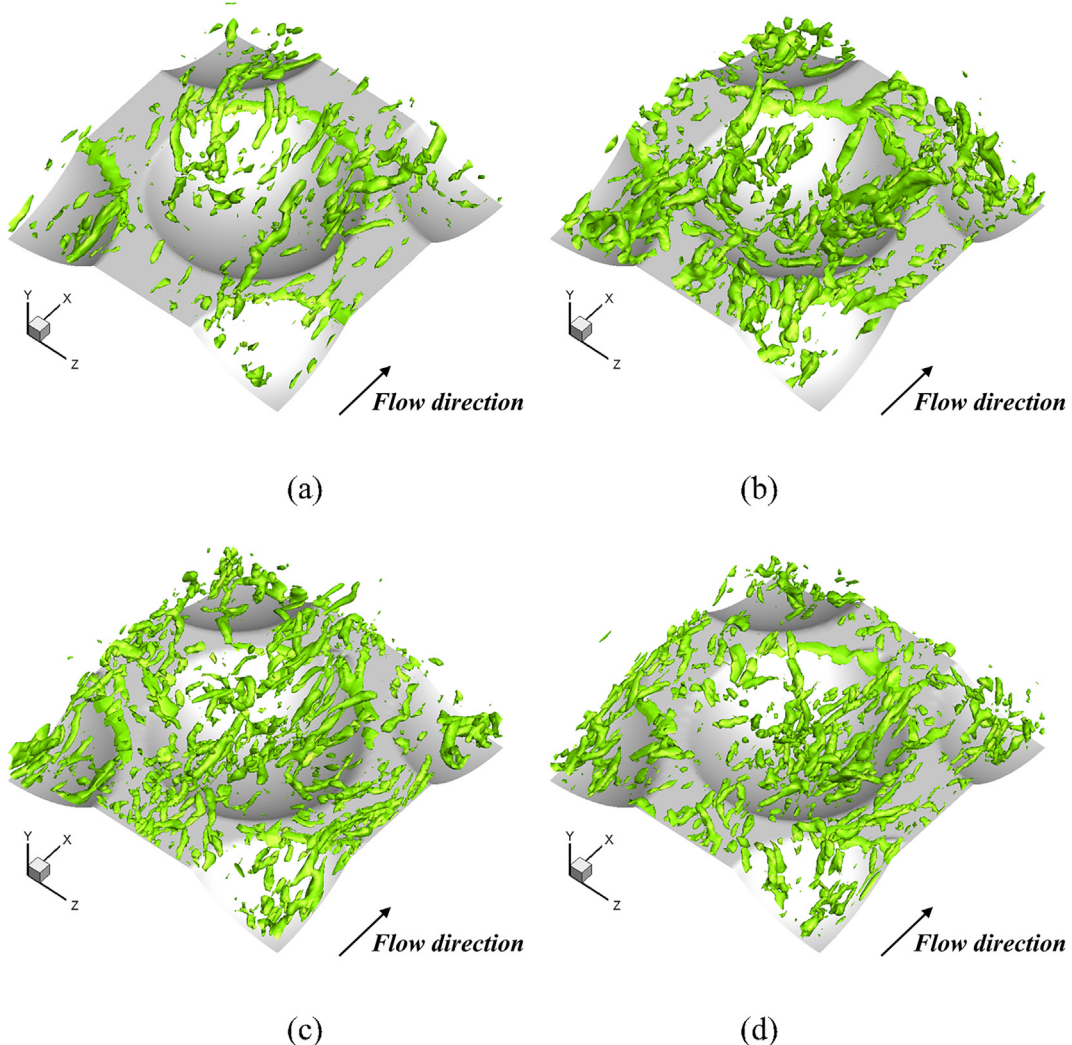


Fig. 5. Three-dimensional vortical structures near the lower surface in instantaneous flow field: (a) general dimpled surface, (b) $\theta = 0^\circ$, (c) $\theta = 15^\circ$, and (d) $\theta = 75^\circ$.

in this study to verify the vortex structure in the channel. In all cases, small-scale eddies are observed near the dimpled surface elongated along the flow direction and inclined toward the diagonal direction, which not only discharged from both sides of the dimple but also flowed into the dimple cavity.

For the general dimpled surface, there are no small-scale eddies near the upstream region of the dimple due to the presence of a recirculation region, as shown in Fig. 5(a). Small-scale eddies are formed downstream of the dimple because the flow impinges against the wall in this region. In the case of $\theta = 0^\circ$, small eddies are generated downstream near the vortex generator due to separation, and these small eddies decrease the recirculation region upstream of the dimple. Many eddies are discharged from upstream to the diagonal direction because the vortex generator changed the flow pattern, as shown in Fig. 5(b). In the cases of $\theta = 15^\circ$ and 75° small-scale eddies are generated and elongated downstream of the vortex generator, as shown in Fig. 5(c) and (d). As the angle between vortex generators increases, the number of small-scale eddies decreases downstream of the vortex generator. Small-scale eddies promote fluid mixing and thus the heat transfer capacity increases in the channel. As the number of these small scale vortices decreases, the flow mixing in the channel decreases. Therefore, the heat transfer decreases with increasing angle inside the vortex generator, as shown in Fig. 4(b). In addition, as the angle between vortex generators increases, the recirculation

region in the upper cavity increases, and the number of small-scale eddies decreases upstream of the dimple.

3.2.2. Time-averaged flow fields

Fig. 6 shows the time-averaged vortex structure with $\lambda_2 = -0.3$. The common phenomenon of the time-averaged vortex structures is the coexistence of streamwise and spanwise vortex structures inside the dimple cavity. For the general dimpled case, there is a spanwise vortex structure at the center of the upstream dimple cavity generated by the flow separation at the upstream rim. There are also a pair of streamwise vortex structures on both sides of the dimple upstream, as shown in Fig. 6(a). In the case of $\theta = 0^\circ$, there are short streamwise vortex structures downstream of the vortex generator due to the separated flow, as shown in Fig. 6(b). The separated flow downstream of the vortex generator increases the pressure drop in the computational domain. As a result, the Fanning friction factor increases compared to the general dimpled surface. The recirculation region of the dimple upstream is reduced because the vortex generator changes the flow into the dimple. Therefore, the size of the spanwise vortex structure in the upstream region of the dimple decreases, and the region of the vortex structure is further confined to the upstream direction.

In the cases of $\theta = 15^\circ$ and 75° , the size of the streamwise vortex structure on both sides of the dimple upstream becomes smaller, as shown in Fig. 6(c) and (d). As the angle inside the vortex

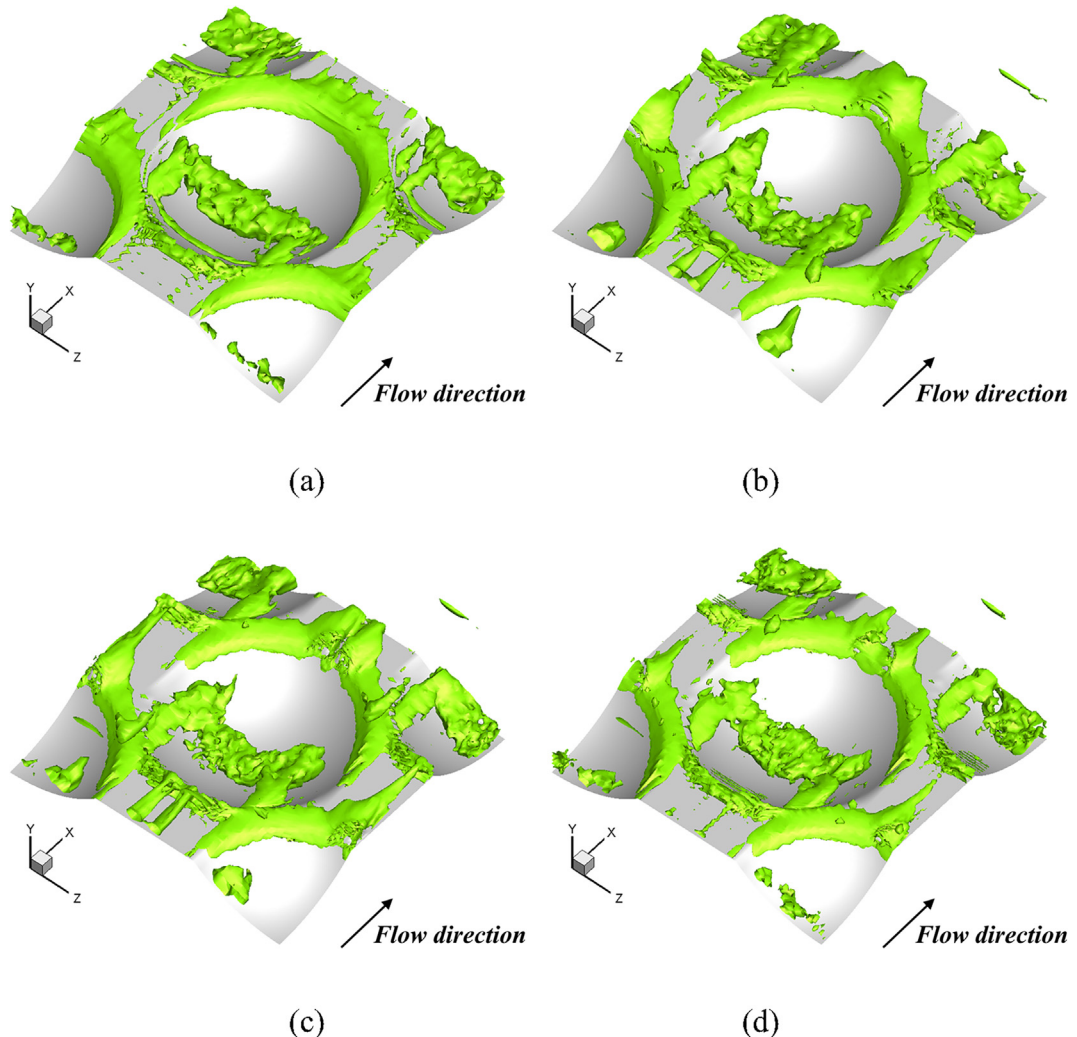


Fig. 6. Three-dimensional vortical structures near the lower surface in time-averaged flow field: (a) general dimpled surface, (b) $\theta = 0^\circ$, (c) $\theta = 15^\circ$, and (d) $\theta = 75^\circ$.

generators increases, the streamwise vortex structure located downstream of the vortex generator is shortened, and the streamwise vortex structure of the dimple upstream is also shortened. Therefore, the pressure drop decreases in the computational domain and consequently the Fanning friction factor also decreases as the streamwise vortex shortened. The spanwise vortex structure of the dimple upstream increases in size as the recirculation region increases and moves toward the center of the dimple.

Fig. 7 shows the distribution of streamlines for different geometries of the lower surface. For all cases, there are recirculation flows inside the dimple cavity and flows in and out of the dimple in the diagonal direction, which are common flow patterns, as previously seen in the vortex structures in **Figs. 5 and 6**. In the case of a general dimpled surface, there is a large spanwise circulation at the center of the upstream dimple cavity, which is a common flow phenomenon inside the general dimpled surface, as shown in **Fig. 7(a)**.

In the case of $\theta = 0^\circ$ shown in **Fig. 7(b)**, the recirculation region in the dimple cavity decreases, and the diagonal flow moves upstream compared to the general dimpled surface due to the variation of the flow pattern as a result of the vortex generator, which was previously seen in the vortex structures in **Figs. 5(b)** and **6(b)**. The flow is sucked from both sides downstream of the vortex generator by flow separation. In the case of $\theta = 15^\circ$, there is a suction region at the downstream of the vortex generator, as in the case of $\theta = 0^\circ$. The recirculation region becomes larger than

at $\theta = 0^\circ$, and the diagonal flow moves more downstream than at $\theta = 0^\circ$.

In the cases of $\theta = 15^\circ$ and 75° , the larger the angle inside the vortex generator, the smaller the suctioned region downstream of the vortex generator is. The recirculation region downstream of the vortex generator disappears at $\theta = 75^\circ$. Furthermore, as the angle inside the vortex generator becomes larger, the effect of the vortex generator on the flow field becomes smaller, and the flow field becomes similar to that of the general dimpled surface. The Fanning friction factor and form drag at $\theta = 0-75^\circ$ in cases with the vortex generator are larger than that of the general dimpled surface due to the recirculation region downstream of the vortex generator, as shown in **Figs. 3 and 4(a)**.

3.3. Plan views of the time-averaged flow and thermal fields

Streamlines on $z = 0$ are shown in **Fig. 8** to show the recirculation region inside the dimple and downstream of the vortex generator. For the general dimpled surface, a recirculation region is formed in the large area of the dimple cavity upstream, as shown in **Fig. 8(a)**. The heat transfer performance is reduced by the large recirculation region located upstream of the dimple cavity in the dimpled channel. Therefore, the general dimpled surface has the lowest heat transfer performance, as shown in **Figs. 3 and 4(b)**. In the case of $\theta = 0^\circ$ shown in **Fig. 8(b)**, the recirculation region of the dimple cavity upstream is decreased in comparison to the general dimpled

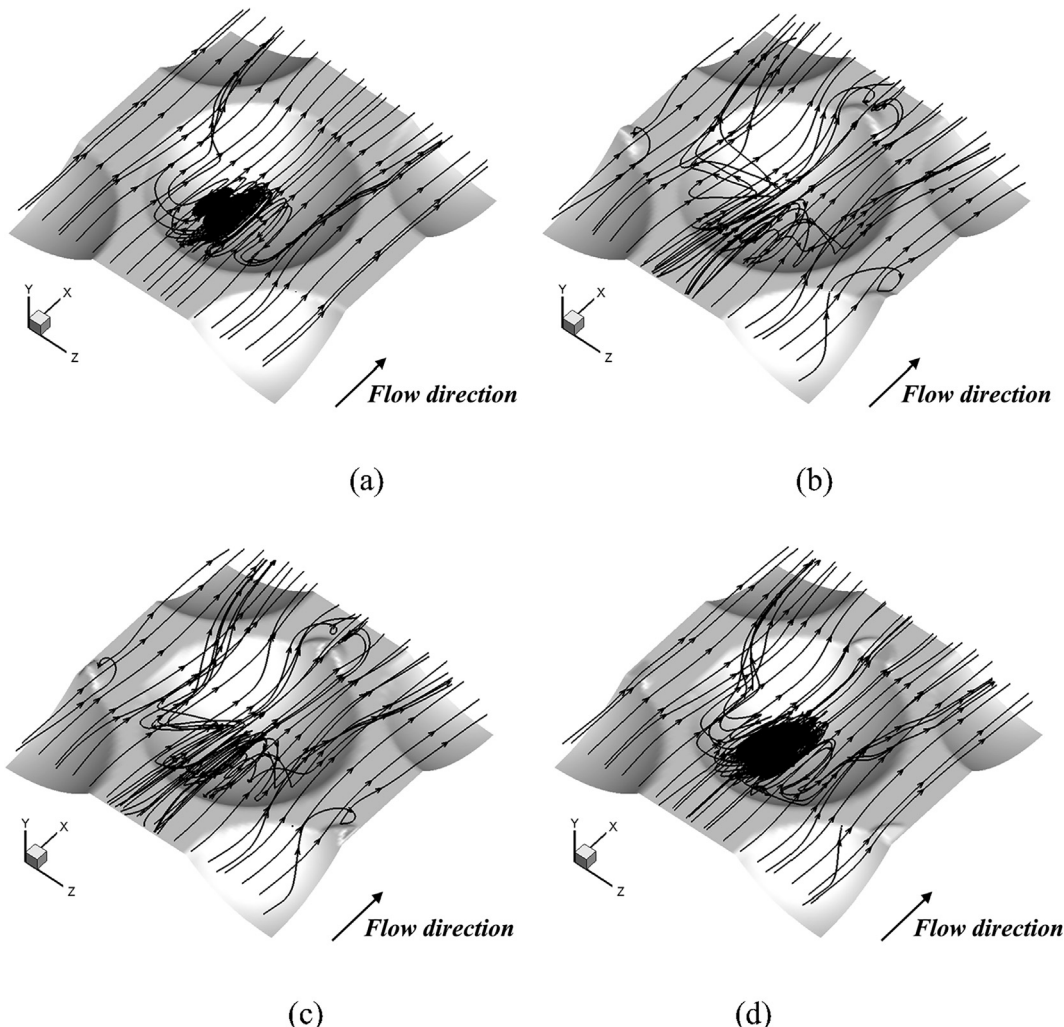


Fig. 7. Three-dimensional streamlines near the lower surface in time-averaged flow field: (a) general dimpled surface, (b) $\theta = 0^\circ$, (c) $\theta = 15^\circ$, and (d) $\theta = 75^\circ$.

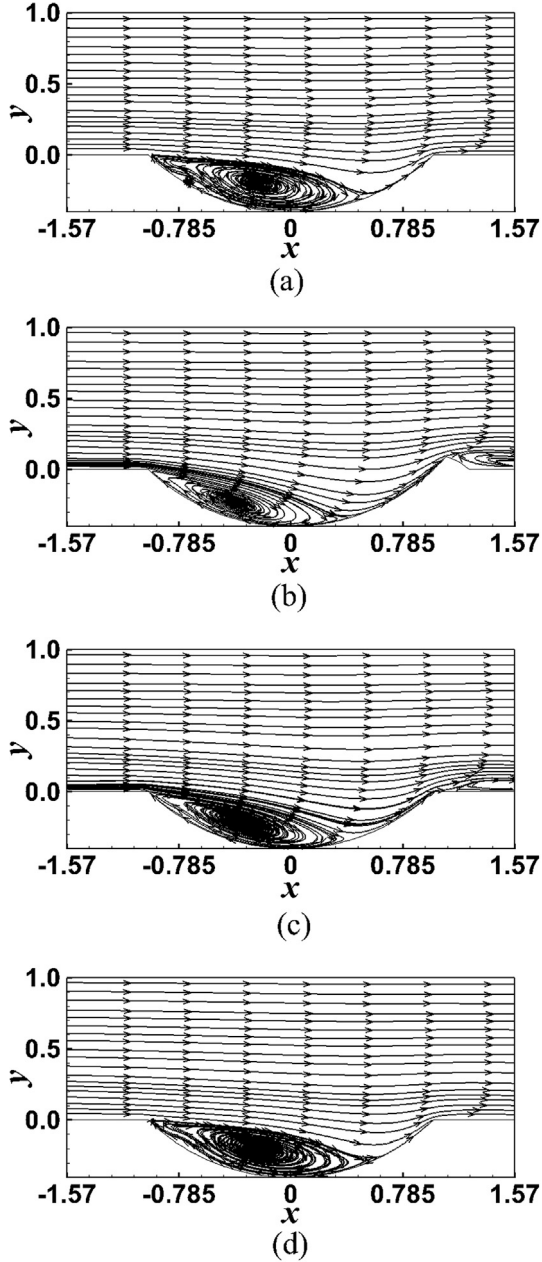


Fig. 8. Two-dimensional streamline on spanwise mid-plane ($z = 0$) for dimpled surface: (a) general dimpled surface, (b) $\theta = 0^\circ$, (c) $\theta = 15^\circ$, and (d) $\theta = 75^\circ$.

surface, and there is a recirculation region after the vortex generator. In the cases of $\theta = 15^\circ$ and 75° , as the angle inside the vortex generator increases, the size of the recirculation region of the dimple cavity increases, and the suction region downstream of the vortex generator decreases, as shown in Fig. 8(c) and (d).

Fig. 9 shows the time-averaged velocity vector fields with iso-thermal lines at $x = 0$. For all cases, there are clockwise and counterclockwise rotation of the streamwise vortices inside the dimple cavity, which can be verified by the time-averaged velocity vector fields of the secondary flow, as shown in Fig. 9(a)–(d). In the cases of $\theta = 0\text{--}75^\circ$, there are secondary vortices over the flat surfaces of both sides of the rim of the dimple, which are clockwise and counterclockwise rotation, as shown in Fig. 9(b)–(d). Therefore, the heat transfer performance for the dimpled surfaces with vortex generator is increased by the enhancement of the flow mixing compared to the general dimpled surface, as shown in Figs. 3 and 4(b).

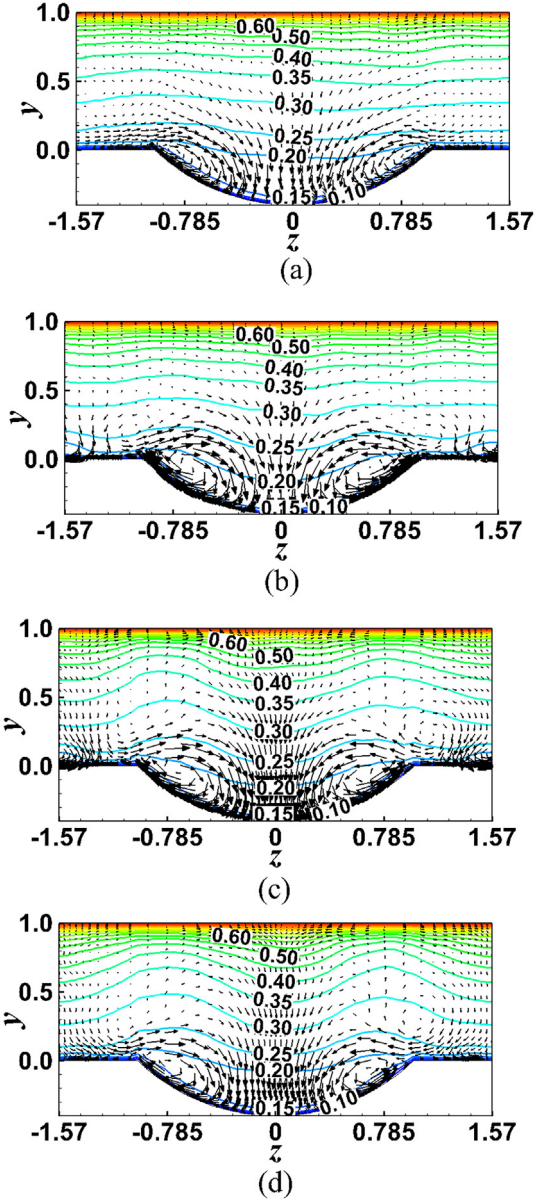


Fig. 9. Iso-thermal lines of the time-averaged thermal field with the superimposed mean velocity vector of the secondary flow on the streamwise-normal plane at $x = 0$: (a) general dimpled surface, (b) $\theta = 0^\circ$, (c) $\theta = 15^\circ$, and (d) $\theta = 75^\circ$.

In the case of the general dimpled surface, small streamwise vortices are located on both sides of the dimple cavity, as shown in Fig. 9(a). In the case of $\theta = 0^\circ$, the streamwise vortices on both sides of the dimple cavity are wider than general dimpled surface, as shown in Fig. 9(b), and a pair of secondary vortices are formed that rotate clockwise and counterclockwise above the lower flat surface. Near $z = -1.57$ and $z = 1.57$, at the center of the lower flat surface, there is a suction flow downstream of the vortex generator due to separation. At $\theta = 15^\circ$, the streamwise vortices on both sides of the dimple become smaller than at $\theta = 0^\circ$. The secondary vortices rotating clockwise and counterclockwise above the lower flat surface are larger than at $\theta = 0^\circ$. Near $z = -1.57$ and $z = 1.57$, the flows that are sucked downstream of the vortex generator are faster than at $\theta = 0^\circ$, as seen in the streamwise vortex structure that is elongated downstream of the vortex generator in Fig. 6(c). The streamwise vortex structure downstream of the vortex generator becomes longer as the flows are suctioned faster. In the cases of $\theta = 15^\circ$ and 75° , as the angle inside the vortex generator increases,

the size of the streamwise vortices on both sides of the dimple cavity is reduced, as shown in Fig. 9(c) and (d). As the angle inside the vortex generator increases, the flow that is suctioned downstream of the vortex generator becomes slower. The streamwise vortex structure becomes shorter as the flow is suctioned more slowly.

For the general dimpled surface, the time-averaged iso-thermal lines are almost uniform in the spanwise direction. In the case of $\theta = 0^\circ$, the heat transfer rate is greatly improved by increasing the isothermal change above the dimple surface. The isotherms in the spanwise direction are distributed in a sinusoidal wave form, in contrast to the results of the general dimple. As the angle inside the vortex generators increases, the isotherm amplitude of the sinusoidal wave increases by the secondary vortices rotating above the lower flat surface.

Fig. 10 shows x -vorticity distributions on the streamwise-normal planes at $x = 0$ and $x = 0.57$. For the general dimpled case, the vorticity regions are separated on the flat plate as fluid flows from $x = 0$ to $x = 0.57$, as shown in Fig. 10(a). However, the intensity of the x -vorticity inside the cavity are almost maintained. For the cases of $\theta = 0\text{--}75^\circ$, as shown in Fig. 10(b)–(d), the vortices generated by the vortex generator on the flat plate are separated into several vortices, and the size and intensity of the vortices are reduced, as

the flow goes downstream. Also, the secondary vortices rotating above the lower flat surface become smaller in size and intensity. For the case of $\theta = 75^\circ$, the effect of vortex generator on the flow field becomes insignificant reflected by the flow field which is found to similar to that of the general dimpled surface. Therefore, x -vorticity distribution is similar to that of the general dimpled surface except the secondary vortices, as shown in Fig. 10(d).

3.4. Mean Nusselt number

Fig. 11 shows the time-averaged local Nusselt number \bar{Nu} on the lower walls for all cases. The time-averaged local Nusselt number is defined as follows:

$$\bar{Nu} = \int_0^{t_p} Nu dt \quad (17)$$

As shown in Fig. 11(a), for general dimpled surface, the highest Nusselt number region can be seen near the downstream of the dimple cavity where the flow is reattached. The lowest Nusselt number region is located in the upstream of the dimple cavity due to recirculation region.

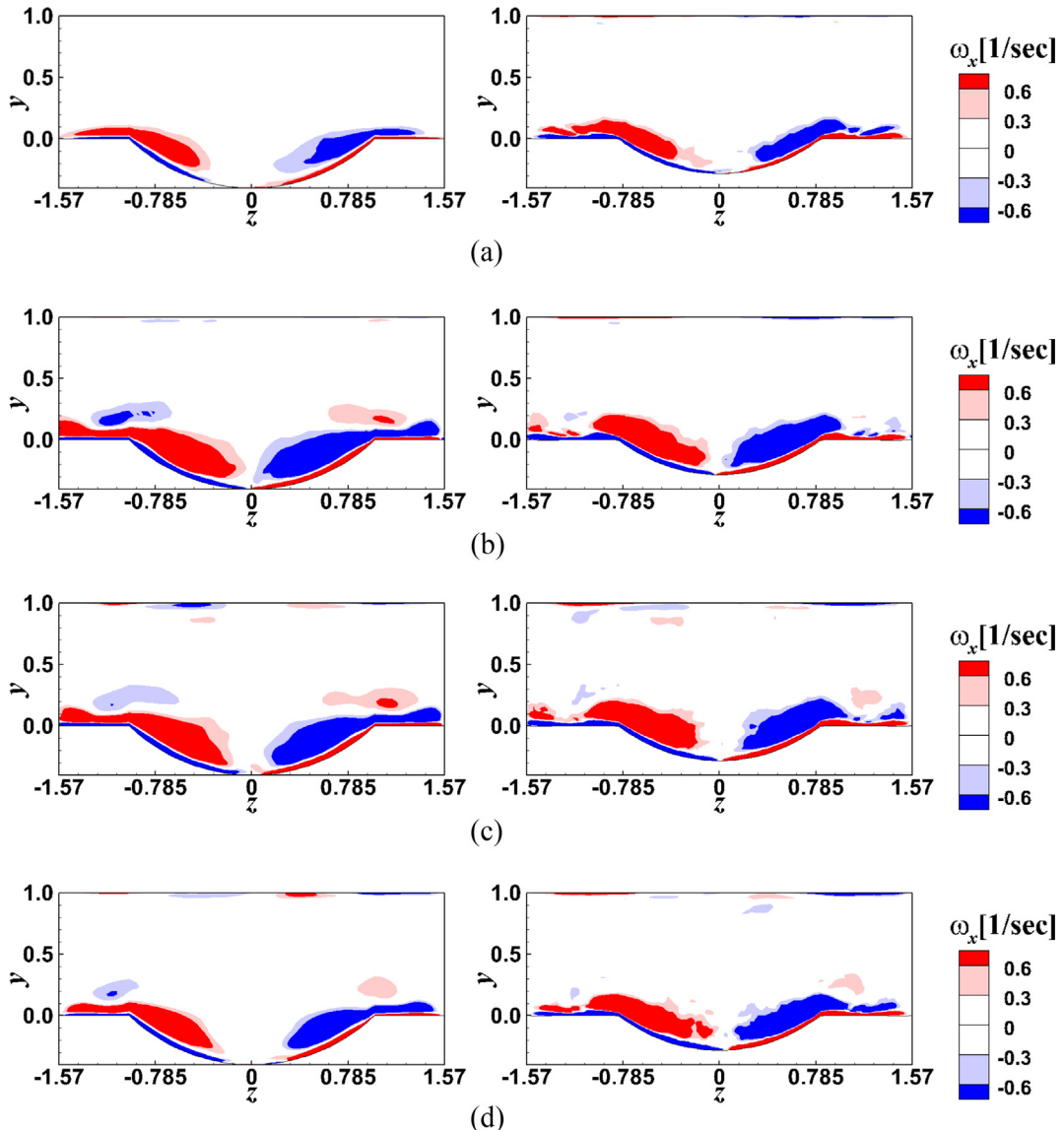


Fig. 10. x -vorticity (ω_x) distribution on the streamwise-normal plane at $x = 0$ and $x = 0.57$: (a) general dimpled surface, (b) $\theta = 0^\circ$, (c) $\theta = 15^\circ$, and (d) $\theta = 75^\circ$.

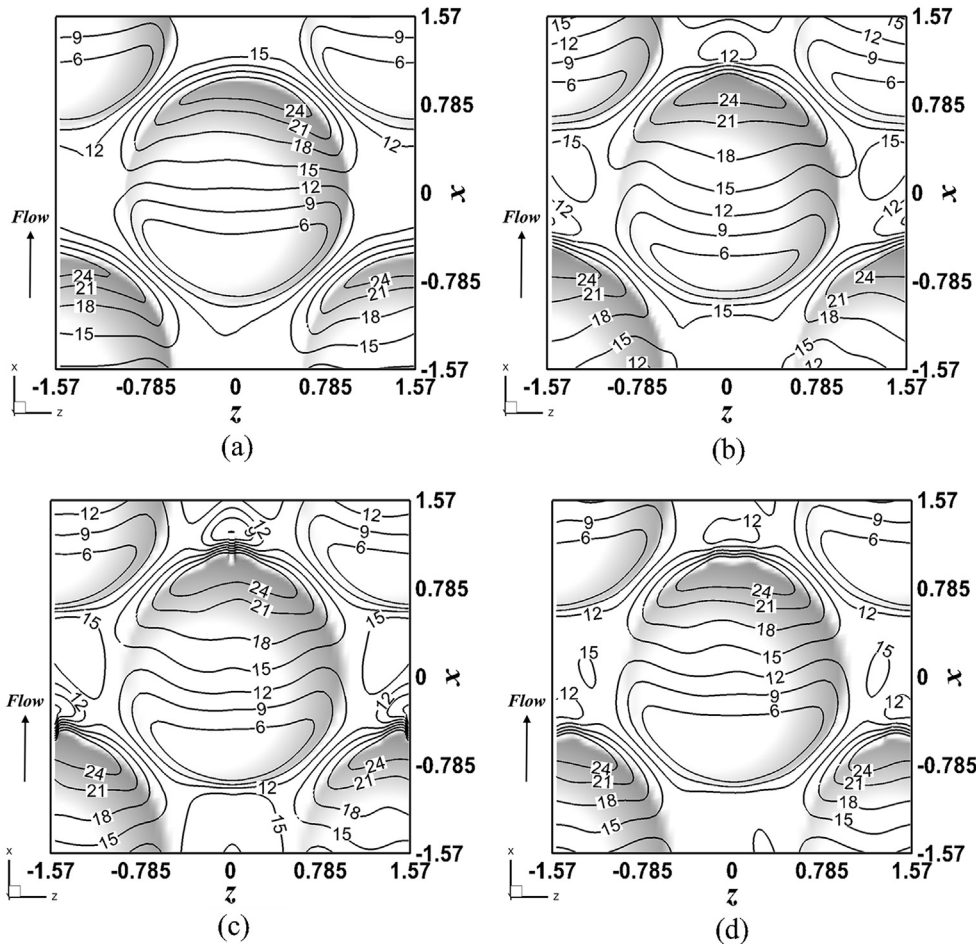


Fig. 11. Distribution of the time-averaged local Nusselt number \bar{Nu} on the lower surface: (a) general dimpled surface, (b) $\theta = 0^\circ$, (c) $\theta = 15^\circ$, and (d) $\theta = 75^\circ$.

For the case with the vortex generator, the heat transfer capacity increases as the recirculation region decreases in the dimple upstream compared to the general dimpled surface. It also has a low Nusselt number distribution on the surface of the vortex generator where flow separation occurs, but it shows a high Nusselt number distribution downstream of the vortex generator by the small vortices, as shown in Fig. 5. Also, x-vorticity with the vortex generator case is found to be larger than that of the general dimpled surface in the computational domain, as shown in Fig. 10. Therefore, the Nusselt number distribution for the dimpled surfaces with vortex generator is increased by the flow mixing compared to the general dimpled surface by the small vortices induced from the vortex generators. Thus, the heat transfer performance is better than that of the general dimpled surface, as shown in Figs. 3 and 4(b). As the angle inside the vortex generator increases, the recirculation region of the dimple upstream becomes larger, and the Nusselt number distribution upstream of the dimple becomes smaller, as shown in Fig. 11(b)–(d). As suction flow downstream of the vortex generator decreases, the Nusselt number distribution becomes lower in this region compared to the case of $\theta = 0^\circ$. Thus, the heat transfer performance is decreased as the angle inside the vortex generator increases, as shown in Figs. 3 and 4(b).

4. Conclusion

This study carried out numerical simulations to investigate the flow and heat transfer characteristics in a dimpled cooling channel

with a vortex generator downstream of the dimple on the lower wall. A small crescent-shaped protrusion was added as a longitudinal vortex generator downstream of the dimple to enhance the heat transfer with less pressure penalty. A direct numerical simulation (DNS) was conducted in a dimpled cooling channel with a Reynolds number and a Prandtl number of 2800 and 0.71. Seven different cases were considered. The results included a description of the flow characteristics through the analysis of the streamlines, vortex structures, and velocity vectors, as well as a description of the thermal characteristics through the local distribution of the Nusselt number.

For the case with vortex generator, the recirculation region in the dimple cavity decreased, and the diagonal flow moved more upstream than with the general dimpled case. The heat transfer capacity then increased as the recirculation region decreased in the dimple upstream compared to the general dimpled case. It also had a low Nusselt number distribution on the surface of the vortex generator where flow separation occurred, but it showed a high Nusselt number distribution downstream of the vortex generator due to the suction flow on both sides of the vortex generator. Thus, the Nusselt number distribution for the cases associated with the vortex generator was higher than that of the general dimple case.

The normalized thermo-performance factors were calculated to estimate the performance of the cooling channel for seven different cases. The normalized thermo-performance factors f/f_0 , j/j_0 , and G_v/G_{v0} decrease as θ increases, as shown in Fig. 3. Among the seven different cases, the highest normalized performance factors were acquired for the case of $\theta = 0^\circ$ to reduce the size of the heat

exchanger. f/f_0 , j/j_0 , and G_v/G_{v0} were respectively about 21%, 11%, and 4% greater for $\theta = 0^\circ$ without a gap in the vortex generator than for the general dimpled surface, as shown in Fig. 3.

Declaration of Competing Interest

The authors declared that there is no conflict of interest.

Acknowledgements

This work was supported by Korea Ministry of Environment (MOE) as the Chemical Accident Prevention Technology Development Project (No. 2015001950002).

References

- [1] Z. Wang, K.S. Yeo, B.C. Khoo, DNS of low Reynolds number turbulent flows in dimpled channels, *J. Turbulence* 7 (2006) 1–31.
- [2] M. van Nesselrooij, L.L.M. Veldhuis, B.W. van Oudheusden, F.F.J. Schrijer, Drag reduction by means of dimpled surfaces in turbulent boundary layers, *Exp. Fluids* 57 (9) (2016) 1–14.
- [3] M.A. Elyyan, A. Rozati, D.K. Tafti, Investigation of dimpled fins for heat transfer enhancement in compact heat exchangers, *Int. J. Heat Mass Transfer* 51 (11–12) (2008) 2950–2966.
- [4] M.A. Elyyan, D.K. Tafti, Large Eddy simulation investigation of flow and heat transfer in a channel with dimples and protrusions, *J. Turbomachinery* (2008) 041016.
- [5] S.Y. Won, Q. Zhang, P.M. Ligrani, Comparisons of flow structure above dimpled surfaces with different dimple depths in a channel, *Phys. Fluids* 17 (4) (2005) 045105.
- [6] N.K. Burgess, P.M. Ligrani, Effects of dimple depth on channel Nusselt numbers and friction factors, *J. Heat Transfer* 127 (8) (2005) 839–847.
- [7] S.Y. Won, P.M. Ligrani, Numerical predictions of flow structure and local Nusselt number ratios along and above dimpled surfaces with different dimple depths in a channel, *Numer. Heat Transfer, Part A: Appl.* 46 (6) (2004) 549–570.
- [8] S.Y. Won, P.M. Ligrani, Flow characteristics along and above dimpled surfaces with three different dimple depths within a channel, *J. Mech. Sci. Technol.* 21 (11) (2007) 1901–1909.
- [9] J. Lan, Y. Xie, D. Zhang, Flow and heat transfer in microchannels with dimples and protrusions, *J. Heat transfer* 134 (2) (2012) 021901.
- [10] N. Sato, M. Inagaki, K. Kaneda, N. Horinouchi, A. Ota, Numerical investigation of the effect of Prandtl number on heat transfer in a dimpled-channel flow, *Int. J. Heat Fluid Flow* 68 (2017) 139–150.
- [11] Y. Xie, H. Qu, D. Zhang, Numerical investigation of flow and heat transfer in rectangular channel with teardrop dimple/protrusion, *Int. J. Heat Mass Transfer* 84 (2015) 486–496.
- [12] H.S. Yoon, S.H. Park, C. Choi, M.Y. Ha, Numerical study on characteristics of flow and heat transfer in a cooling passage with a tear-drop dimple surface, *Int. J. Therm. Sci.* 89 (2015) 121–135.
- [13] C.N. Jordan, L.M. Wright, Heat transfer enhancement in a rectangular ($AR=3:1$) channel with V-shaped dimples, in: ASME 2011 Turbo Expo: Turbine Technical Conference and Exposition. American Society of Mechanical Engineers, 2011, pp. 1505–1516.
- [14] G. Xie, J. Liu, P.M. Ligrani, W. Zhang, Numerical predictions of heat transfer and flow structure in a square cross-section channel with various non-spherical indentation dimples, *Numer. Heat Transfer, Part A: Appl.* 64 (3) (2013) 187–215.
- [15] J.H. Doo, H.S. Yoon, M.Y. Ha, Study on improvement of compactness of a plate heat exchanger using a newly designed primary surface, *Int. J. Heat Mass Transfer* 53 (25–26) (2010) 5733–5746.
- [16] Y. Rao, C. Wan, Y. Xu, An experimental study of pressure loss and heat transfer in the pin fin-dimple channels with various dimple depths, *Int. J. Heat Mass Transfer* 55 (2012) 6723–6733.
- [17] Y. Rao, C. Wan, Y. Xu, S. Zang, Spatially-resolved heat transfer characteristics in channels with pin fin and pin fin-dimple arrays, *Int. J. Therm. Sci.* 50 (2011) 2277–2289.
- [18] P.M. Ligrani, C.S. Subramanian, D.W. Craig, P. Kaiswan, Effects of vortices with different circulations on heat transfer and injectant downstream of a row of film-cooling holes in a turbulent boundary layer, *J. Heat Transfer* 113 (1) (1991) 79–90.
- [19] P.M. Ligrani, C.S. Subramanian, D.W. Craig, P. Kaiswan, Effects of vortices with different circulations on heat transfer and injectant downstream of a single film-cooling hole in a turbulent boundary layer, *J. Turbomach.* 113 (3) (1991) 433–441.
- [20] A. Sinha, H. Chattopadhyay, A.K. Iyengar, G. Biswas, Enhancement of heat transfer in a fin-tube heat exchanger using rectangular winglet type vortex generators, *Int. J. Heat Mass Transfer* 101 (2016) 667–681.
- [21] M. Khoshvagh-Aliabadi, S. Zangouei, F. Hormozi, Performance of a plate-fin heat exchanger with vortex-generator channels: 3D-CFD simulation and experimental validation, *Int. J. Therm. Sci.* 88 (2015) 180–192.
- [22] L.H. Tang, W.X. Chu, N. Ahmed, M. Zeng, A new configuration of winglet longitudinal vortex generator to enhance heat transfer in a rectangular channel, *Appl. Therm. Eng.* 104 (2016) 74–84.
- [23] Z. Ke, C. Chen, K. Li, S. Wang, C. Chen, Vortex dynamics and heat transfer of longitudinal vortex generators in a rectangular channel, *Int. J. Heat Mass Transfer* 132 (2019) 874–885.
- [24] L. Luo, F. Wen, L. Wang, B. Sundén, S. Wang, On the solar receiver thermal enhancement by using the dimple combined with delta winglet vortex generator, *Appl. Therm. Eng.* 111 (2017) 586–598.
- [25] H.H. Xia, G.H. Tang, Y. Shi, W.Q. Tao, Simulation of heat transfer enhancement by longitudinal vortex generators in dimple heat exchangers, *Energy* 74 (2014) 27–36.
- [26] J. Kim, P. Moin, Application of a fractional-step method to incompressible Navier-Stokes equations, *J. Comput. Phys.* 59 (2) (1985) 308–323.
- [27] Y. Zang, R.L. Street, J.R. Koseff, A non-staggered grid, fractional step method for time-dependent incompressible Navier-Stokes equations in curvilinear coordinates, *J. Comput. Phys.* 114 (1) (1994) 18–33.
- [28] R.K. Shah, A.L. London, *Laminar Flow Forced Convection in Ducts: A Source Book for Compact Heat Exchanger Analytical Data*, Academic Press, 2014.
- [29] J. Jeong, F. Hussain, On the identification of a vortex, *J. Fluid Mech.* 285 (1995) 69–94.